SPRINGER LINK

Log in

☰ Menu　　　🔍 Search　　　🛒 Cart

Nanocrystalline $Ni_{0.70-x}Cu_xZn_{0.30}Fe_2O_4$ with $0 \leq x \leq 0.25$ prepared by nitrate–citrate route: structure, morphology and electrical investigations

Download PDF ⤓

**Journal of Materials Science: Materials in Electronics**

Aims and scope

Submit manuscript

Ashok V. Humbe ✉, Prashant B. Kharat, Anant C. Nawle & K. M. Jadhav

Abstract

The structure, morphology, temperature dependent electrical and frequency dependent dielectric behavior of Cu^{2+} substituted Ni−Zn spinel ferrite nanoparticles having generic formula $Ni_{0.70-x}Cu_xZn_{0.30}Fe_2O_4$ (x = 0.00, 0.05, 0.15 and 0.25) prepared by sol−gel auto combustion technique with citric acid as a chelating agent is reported here. The XRD patterns revealed the presence of cubic spinel structure. The crystallite size was obtained using Scherrer's formula which varies between 29 and 34 nm. The lattice parameter was found to increase with an increase in copper concentration. FTIR spectra show the characteristic bands for tetrahedral and octahedral sites. The morphology

investigated by SEM technique demonstrates the nanocrystalline grain formation with almost spherical geometry. The grain size obtained from SEM analysis is in the range of 69−88 nm. The particle size obtained through TEM image analysis varies from 30 to 35 nm. The electrical and dielectric behavior was studied using a two-probe technique as a function of temperature and frequency respectively. Various electrical parameters like DC resistivity, activation energy, drift mobility, charge carrier concentration, diffusion coefficient were obtained as a function of copper concentration 'x'. Arrhenius plot indicates the semiconducting nature of Cu^{2+} substituted Ni−Zn spinel ferrite. The dielectric constant and dielectric loss tangent both decreases with increase in frequency and concentration of Cu^{2+}.

Similar content being viewed by others
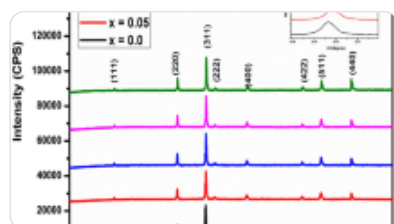
Effect of Al3+ substitution on the synthesis, magnetic, and electrical properties of Ni0.3Zn0.5Co0.2Fe2−xAlx...

Article | 15 November 2023
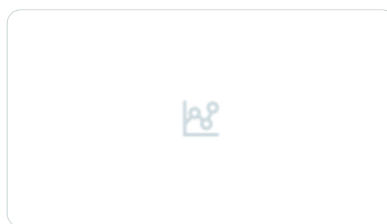
Synthesis and Characterization of Polyol–Assisted Nano Cu0.2Ni0.2Sn0.2Ba0.4...

Article | 28 March 2017

Structural, Magnetic, and Electrical Properties of Ni0.65Zn0.35−x Cu x Fe2 O 4 Nanoferrite System

Article | 28 May 2015

Use our pre-submission checklist →

Avoid common mistakes on your manuscript.

1 Introduction

Ferrites are ferrimagnetic ceramic materials with iron III oxide as their main component along with metal oxides. They exhibit a wide range of electromagnetic properties useful for a variety of technological applications. The most common ferrites are spinel type ferrite with the general formula MFe_2O_4 where, M is a divalent metal ion like Ni^{2+}, Co^{2+}, Cu^{2+}, etc. Over the past decade, spinel ferrites have grown tremendously as interesting magnetic nanoparticles. These magnetic nanoparticles have been studied to illustrate the effects of nanoscale finite size on the structure, morphology and its electric as well as dielectric behavior. They have been widely studied since they offer the major

advantages due to their unique size as well as excellent physicochemical properties. The spinel ferrite nanoparticles can be used in various technological applications such as gas sensing, magnetic resonance imaging, ferrofluids, cancer therapy, drug delivery systems, electrical and electronic devices [1,2,3,4,5,6,7] etc. The high permeability, high magnetization and high resistivity, low core and dielectric losses are the remarkable properties of spinel ferrite which makes them useful in many new domains of technological applications. The interesting electrical and dielectric properties of spinel ferrite nanoparticles depend mainly on synthesis techniques. The wet chemical methods like sol−gel, co-precipitation, thermal decomposition, micro-emulsion, reverse micelle, hydrothermal [8,9,10,11,12,13,14] etc was effectively used for the synthesis of spinel ferrite nanoparticles. Among these synthesis methods, sol−gel auto combustion is the most preferred method as it offers many advantages like homogeneity at an atomic scale, fine particle size distribution, requires low temperature, offers good chemical stability, high yield, easy and cost effective compared to other synthesis methods. However, the selection of fuel, metal nitrate to fuel ratio, pH, annealing temperature etc synthesis parameters has to be taken care in order to obtain the good nanocrystalline particles. Apart from the synthesis method suitable choice of dopant, its ionic size, valency, site preference and amount of doping affects the structural, electrical and dielectric properties of nanocrystalline spinel ferrite nanoparticles.

In the literature, pure (cobalt, nickel etc.) [15, 16] as well as mixed (Ni−Zn, Cu−Zn, etc.) [17, 18] spinel ferrites in nanocrystalline form have been studied by many researchers with a view to understand their electro-magnetic behavior at a nanoscale. The substitution of copper ions in Ni−Zn spinel ferrite at nickel site (octahedral) is reported in the literature for few concentrations [19,20,21]. Their studies revealed that on copper doping, the structural, electrical and magnetic properties were influenced. Many of the researchers have studied NiCuZn spinel ferrite for multilayer chip inductor application and other applications such as high frequency devices. The divalent ions such as Co^{2+}, Cu^{2+}, Mg^{2+} [22,23,24] etc doping to Ni−Zn spinel ferrite may lead to interesting properties. The substitution of Cu^{2+} in Ni−Zn spinel ferrites make them suitable for miniaturization of electronic components and fabrication of integrated electronic devices such as an inductor, transformer, phase shifter, memory etc. The recent discoveries of giant magneto resistance, macroscopic quantum tunnelling, etc have attracted additional attention to nanosized Ni−Zn spinel ferrites for their use in magnetic tape recording and magneto-optic devices. It is worth to mention here that if Cu^{2+} is doped in Ni−Zn spinel ferrite it can reduce the sintering temperature. Further it may enhance the density as well as the crystalline growth and electrical resistivity. Hence, the prepared material may be useful for microwave applications.

The aim of the present work was to synthesize single phase NiCuZn nanoparticles using sol−gel auto combustion method with metal nitrates as oxidants and citric acid as a fuel. Further, to study the

effects of copper substitution on structure, morphology, electrical and dielectric properties of Ni−Zn spinel ferrite nanoparticles using XRD, FTIR, SEM and HR-TEM characterizations and electrical as well as dielectric measurements for potential application in some electrical and electronic devices.

2 Experimental

NiCuZn ferrites with a composition of $Ni_{0.70-x}Cu_xZn_{0.30}Fe_2O_4$ (x = 0.00, 0.05, 0.15 and 0.25) were synthesized by sol−gel auto combustion method. The oxidants as nickel nitrate [$(Ni(NO_3)_2 \cdot 6H_2O$], copper nitrate [$Cu(NO_3)_2 \cdot 6H_2O$], zinc nitrate [$Zn(NO_3)_2 \cdot 6H_2O$], ferric nitrate [$Fe(NO_3)_3 \cdot 9H_2O$] and citric acid ($C_6H_8O_7$) as fuel in analytical-grade were used as raw materials. In order to release maximum energy, the total valencies of metal nitrates to that of fuel must be balanced. Thus, according to propellant chemistry [25], the metal nitrate to fuel ratio was calculated and chosen as 1:3 (metal nitrate:citric acid). The stoichiometric amounts of metal nitrates (Ni, Cu, and Zn), ferric nitrate and citric acid (1:2:3) were weighed and then dissolved in distilled water separately. The mixed solution of all the raw materials was taken in a glass beaker and kept on a hot plate with temperature of 90 °C and stirred around 400 rpm. On gel formation, the temperature was further increased to 120 °C. When all the water molecules evaporated, the viscous gel began to bubble, within few seconds it started to ignite and burnt with the glowing flints. The process of auto-combustion was completed within few seconds by yielding the fluffy ash. The as-prepared powder was annealed at 600 °C for 6 h and then cooled to room temperature in the air atmosphere using programmable muffle furnace (Thermolyne-1500).

3 Characterizations

The crystallographic properties were characterized by Philips X-ray diffractometer (XRD, Cu target, Kα radiation, 40 kV, and 40 mA). FTIR studies were performed by Perkin Elmer spectrometer in the range of $400-4000 \text{ cm}^{-1}$. The microstructure of samples was observed by scanning electron microscopy (SEM, JEOLJSM-6490L), from SEM micrographs the average grain size (D) was estimated. The elemental composition was investigated by energy dispersive spectrum (EDS) technique attached with SEM. The morphology and particle size distribution were performed using high-resolution transmission electron microscopy (FEI, technai G2 F20). The DC electrical resistivity and dielectric measurements were carried out by two-probe technique as a function of temperature in the temperature range from room temperature-850 k and as a function of frequency in the range of 50 Hz to 1 MHz respectively. Both the measurements were performed on disc shaped pellets of dimensions 12 mm × 3 mm. During measurements both the surfaces of pellet were silver pasted for good ohmic contact. The DC electrical measurements were used to obtain the electrical parameters such as DC resistivity, activation energy, drift mobility, charge carrier concentration, diffusion coefficient. Using

values of capacitance, the dielectric constant was determined for each sample. Both dielectric constant and dielectric loss tangent were also studied for varying concentration of divalent copper ions.

4 Results and discussion

4.1 TGA–DTA

The minimum required temperature for the complete decomposition can be estimated from the thermal behavior of as-prepared powder. It is treated as a minimum temperature for annealing the prepared material to have better crystallization and or to remove the nitrate impurity if any remained. TGA-DTA curve for a typical sample x = 0.15 is shown in Fig. 1. The TGA-DTA curves were recorded in the temperature range from room temperature – 800 °C with the rate of 10 °C/min in the air atmosphere. It is observed from TGA curve that the combustion process was carried out through three stages with the total weight loss of 11.5%. The first stage (20−94 °C) can be attributed to vaporization of trapped water molecules followed by decomposition of citric acid in the second stage (95−285 °C). The final stage in the temperature range (286−596 °C) show the sustained mass loss of 5.4% which can be presumed to the crystallization of the ferrite. Beyond the temperature 597 °C the TGA curve exhibits the flat response indicating no significant weight loss which suggests the formation of the ferrite phase. Furthermore, DTA curve exhibits two exothermic humps centered at 175 and 490 °C. The peak at 175 °C can be attributed to the decomposition of citric acid while broad hump at 490 °C is to be attributed to auto combustion reaction. During this reaction the removal of nitrates takes place and the formation of ferrite phase occurred. This study hints the formation temperature of the NiCuZn spinel ferrite is ~ 500 °C. Our results are analogous to that of reported spinel ferrite nanoparticles [26].

Fig. 1
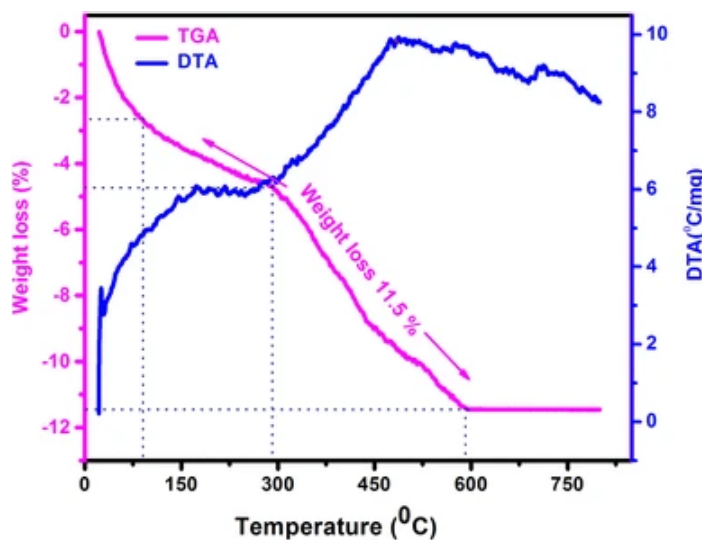
TGA–DTA plot for a typical sample x = 0.15

4.2 Structural characterizations

4.2.1 XRD

Figure 2 shows the X-ray diffraction patterns of the annealed $Ni_{0.70-x}Zn_{0.30}Fe_2O_4$ (x = 0.00, 0.05, and 0.15) nanoparticles recorded at room temperature using Cu-kα radiation. The XRD patterns show the Bragg reflections (220), (311), (222), (400), (422), (511), and (440). All these reflections belong to cubic symmetry. The analysis of XRD patterns favored the formation of all samples with single phase cubic spinel structure. Our XRD patterns are in close agreement with other XRD patterns of Ni−Zn spinel ferrite of JCPDS-22-1119. The inset in Fig. 2 shows a broadened peak of the most intense peak (311) which was used to calculate the crystallite size. The crystallite size for each sample was calculated using Scherrer's formula (t = 0.9/cos, where the symbols have their usual meanings). The crystallite size varies in between 29 and 34 nm. The obtained values of crystallite size are given in Table 1 which confirms the nanocrystalline nature of all the prepared samples.

Fig. 2
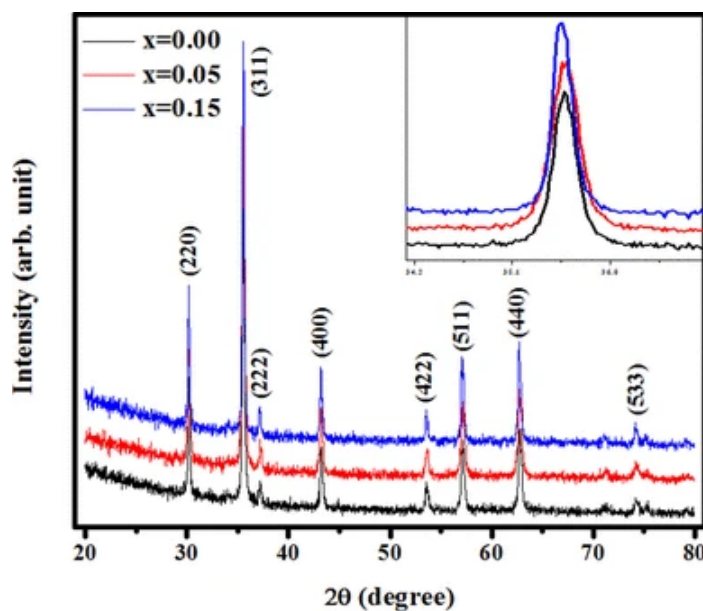
XRD patterns of $Ni_{0.70-x}Cu_xZn_{0.30}Fe_2O_4$ (x = 0.00, 0.05 and 0.15)

Table 1 Structural parameters as lattice parameter (a), X-ray density (d_x), bulk density (d_B), porosity (P), crystallite size (t) and hopping lengths (L_A and L_B)

The values of interplanar spacing d and Miller indices (h k l) were used to estimate the values of lattice parameter (a). The lattice parameter of all the samples was calculated using the standard relation a = d √N and their values are given in Table 1. It is evident from Table 1 that the lattice parameter increases with increase in copper substitution 'x'. The increase in the lattice parameter is linear obeying Vegard's law and can be attributed to the larger ionic radius of Cu^{2+} (0.67 Å) ions as compared to Ni^{2+} (0.64 Å) ions. A similar variation of lattice parameter is reported in the literature for other NiCuZn spinel ferrite [27].

The X-ray density was calculated using the relation $d_x = 8M/N_A a^3$ where, M is the molecular weight of the sample, N_A is the Avogadro's number and a^3 is the unit cell volume. The increase in X-ray density was observed as copper substitution increases which may be due to the fact that the increase in molecular weight overtakes the increase in volume, thus X-ray density increases. The values of the X-ray density and bulk density are tabulated in Table 1. It is observed that the bulk density d_B is less than X-ray density d_x, the difference between the X-ray density and bulk density is due to the existence of inter and intra granular porosity of the samples.

The percentage porosity was obtained from the values of the X-ray density and bulk density using the relation P = $(d_x - d_B)/d_x$ and presented in Table 1. It is observed from Table 1 that the percentage porosity varies from 35 to 37%.

The XRD data was also used to determine other structural parameters like hopping length for tetrahedral and octahedral sites. The hopping length for tetrahedral A–site and octahedral B–site was calculated using following relations

$${{\text{L}}_{\text{A}}}={\text{a}}\surd \left(3\right){{/4{\AA}}}$$

(1)

$${\text{L}}_{{\text{B}}} = {\text{a}}\surd \left(2 \right)/4{\AA}$$

(2)

The values of hopping length obtained by using above relations are given in Table 1. It is observed from this table that, like lattice parameter hopping length for tetrahedral (A) and octahedral [B] site increases with increasing copper substitution.

4.2.2 FTIR

FTIR spectra of annealed samples of concentration x = 0.00, 0.05, 0.15 and 0.25 were recorded in the range of 400−4000 cm^{-1} at room temperature and shown in Fig. 3. It reveals the prominent peaks below wavenumber 1000 cm^{-1} which are the common features of the formation of spinel ferrite skeleton. These peaks are the characteristic features of spinel ferrites and are attributed to the stretching and bending vibrations due to interactions between cations and oxygen atoms at tetrahedral (A) and octahedral [B] sites. Also, the changes in bond lengths of Fe−O at tetrahedral (A) site and octahedral [B] site results into the difference in the band values.

Fig. 3
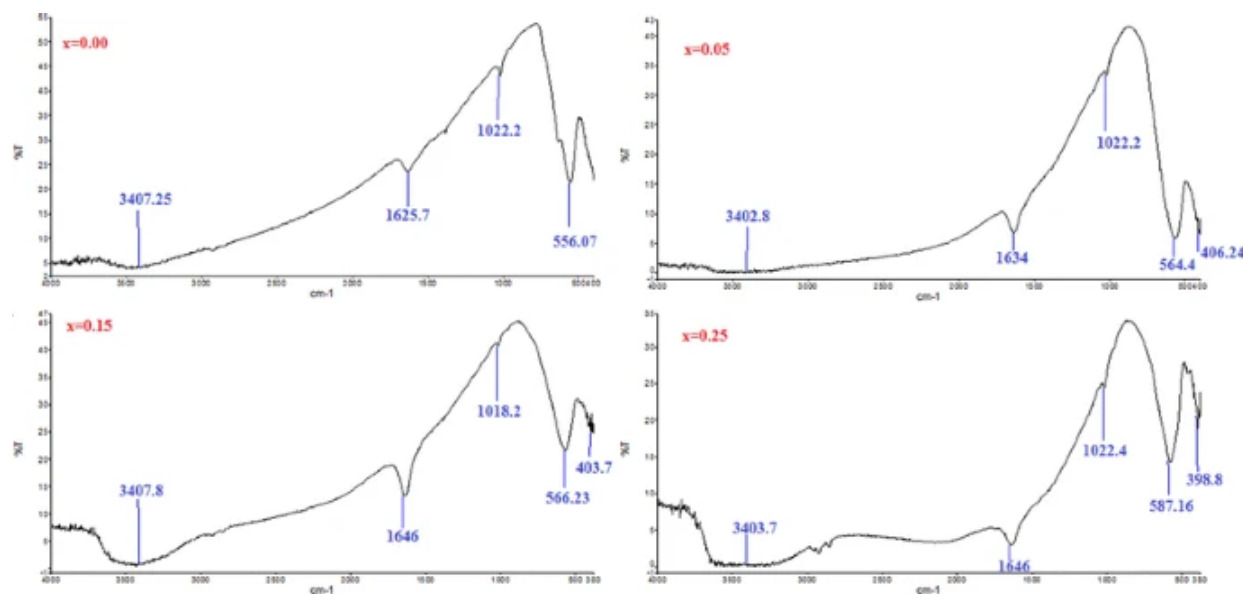
FTIR spectra of $Ni_{0.70-x}Cu_xZn_{0.30}Fe_2O_4$ (x = 0.00, 0.05, 0.15 and 0.25)

In the FTIR spectra of each sample, the broad band near 3400 and 1630 cm^{-1} are observed. This can be due to stretching and bending vibrations of O−H of the free or absorbed water, suggesting the presence of hydroxyl group in the present samples. The water may be absorbed due to large volume to surface ratio of the sample. The similar results are seen in the reports [28]. The band observed at 1022 cm^{-1} in each spectrum is attributed to metal-alloy. The two prominent absorption bands in the range of 556−587 and 406−398 cm^{-1} are observed. These bands are the common features of spinel ferrites [29] and

are attributed to Fe−O bond. The observed difference in band positions is expected because of the differences in distances of Fe−O for both tetrahedral A-site (1.865 Å) and octahedral B-site (2.02 Å) [30]. This can be interpreted by the stronger bonding at the A-site than that of at the B-site. In conclusion, it is the formation of ferrite skeleton. The values (Fig. 3) of band position as υ_1 and υ_2, which reveals that the higher frequency absorption bands were shifted towards higher frequency while that of lower frequency shifted towards lower frequency. This can be a consequence of the increase in particle size. It is worth to mention here that, for nanoparticles the change in chemical group environment leads to change in the vibration frequency of that group.

4.3 Morphology

4.3.1 SEM−EDS

The SEM micrographs as well as EDS spectra of the samples x = 0.00, 0.05 and 0.15 are shown in Fig. 4. The morphology of the studied samples was investigated using SEM images. The primary analysis of SEM images indicates the grains of varying sizes, a fluffy morphology and sponge-like porous structure. The observed morphology is similar to that of reported for nanocrystalline spinel ferrites [31] prepared by wet chemical route. It is worth to mention here that the porous structure has a large specific surface area which indicates a much more active surface area useful for various technological applications. Further, it is observed from Fig. 4 that the grain size is not uniform indicating the possibility of agglomeration of nanoparticles. The estimated average grain size is 69, 74 and 88 nm for x = 0.00, 0.05 and 0.15 respectively which suggests the nanocrystalline nature of the NiCuZn spinel ferrites. The increase in grain size with increasing Cu content 'x' can be attributed to the liquid phase formation during annealing which results in increase of grain size [27].

Fig. 4
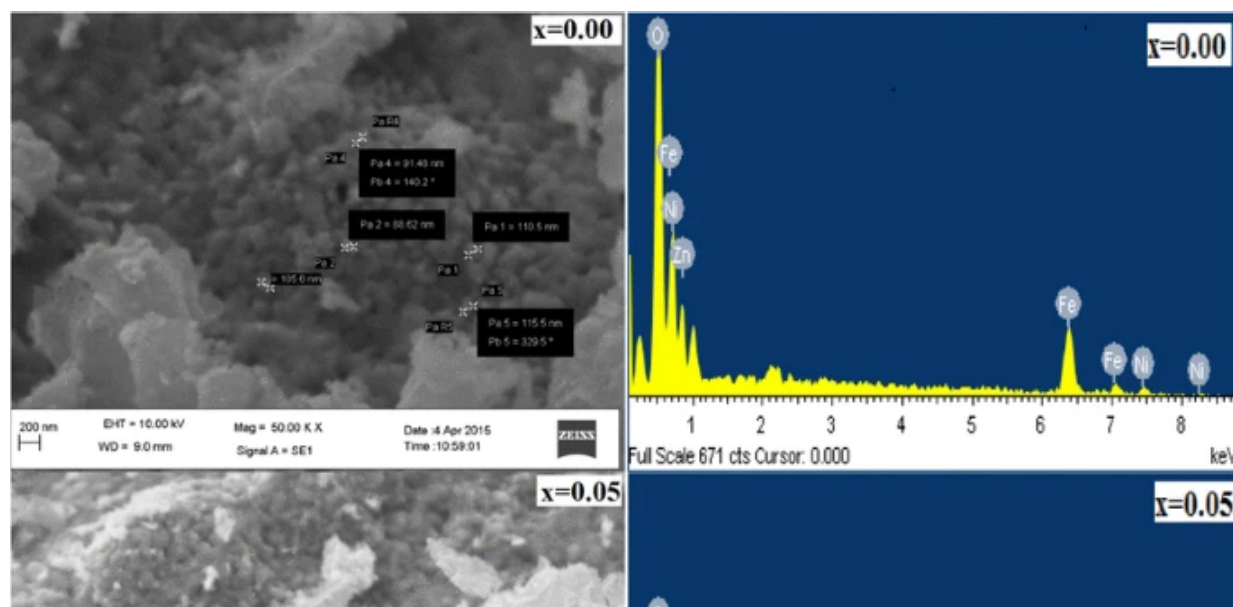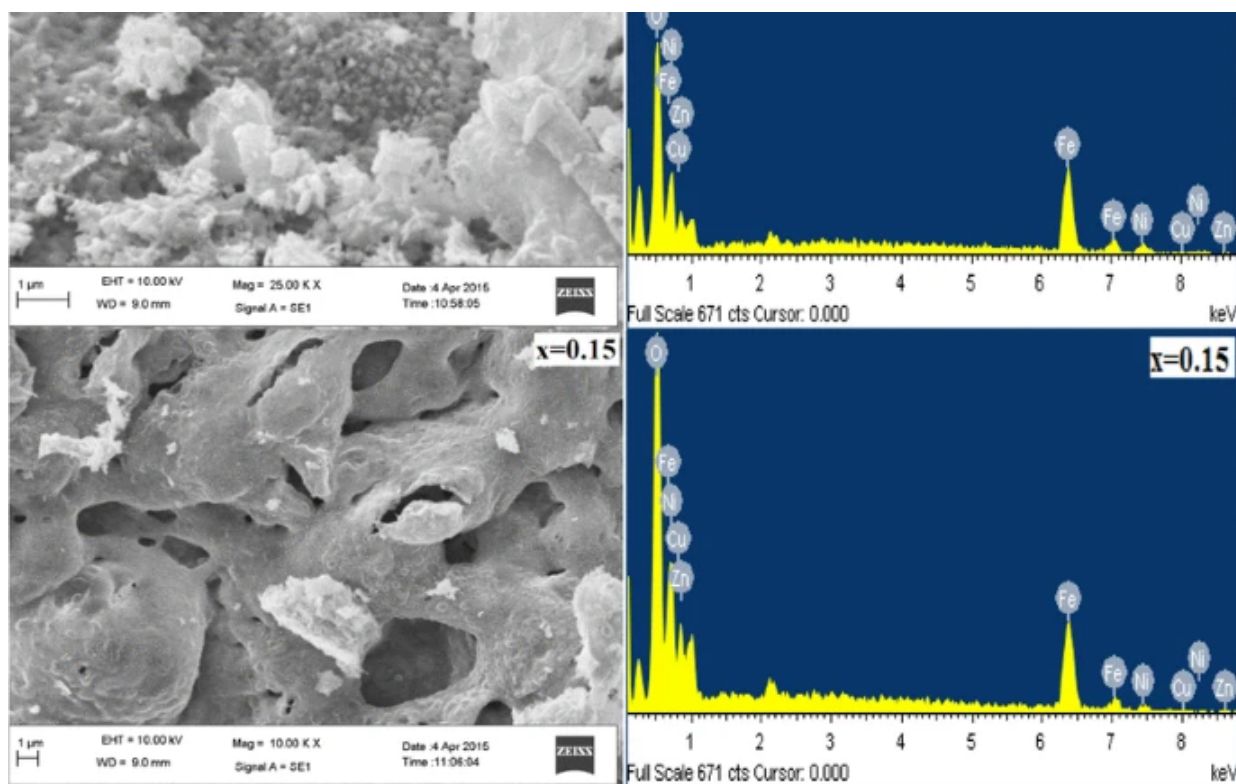
SEM images and EDS spectra of $Ni_{0.70-x}Cu_xZn_{0.30}Fe_2O_4$ (x = 0.00, 0.05, and 0.15)

An elemental composition of each sample was determined by employing EDS technique. EDS spectra of samples are presented in Fig. 4. An EDS spectrum of sample x = 0.00 shows the peaks of Ni, Zn, Fe and O. The peak for Cu appeared in remaining samples and its percentage was found to increase with copper content 'x'. The stoichiometry estimated by EDS spectra is very close to that of theoretically anticipated values. It is worth to state that the formation of NiCuZn spinel ferrite using sol−gel auto-combustion assisted by citric acid has fully favored. Furthermore, the energy supplied during reaction has homogeneously distributed through the used oxidants which completely converted and formed NiCuZn spinel ferrite.

4.3.2 TEM–SAED

The TEM images, particle size distribution, SAED patterns of x = 0.00, 0.05, and 0.15 and HR–TEM images of sample x = 0.00 as well as 0.15 are depicted in Figs. 5, 6, 7. It demonstrates that each image consists of spherical nanoparticles and has a narrow size distribution. It is clearly observed that the separate as well as the agglomeration to certain extent of the particles is present. The agglomerations can be attributed to the high surface area of magnetic nanoparticles. Similar results for ferromagnetic spinel ferrites were observed as reported in [32]. The average particle size estimated by Gaussian of all particles in each image as shown in Figs. 5, 6, 7 is 30, 32 and 35 nm for x = 0.00, 0.05 and 0.15 respectively. The estimated average particle size of each sample is in close agreement with that of

calculated by XRD. Also, from SAED patterns it is observed that they are similar to each other and the diffraction rings are well consistent with the hkl planes present in the cubic spinel structure. Furthermore, the superposition of bright spots on Debye rings in SAED patterns suggests a polycrystalline structure of NiCuZn system. The corresponding HR–TEM images of x = 0.00 and 0.15 ferrite nanoparticles were used to estimate the distance between lattice fringes. The values of inter-planar distance are 0.18 and 0.24 nm which are corresponding to 422 and 222 planes verified with that of given by XRD data.
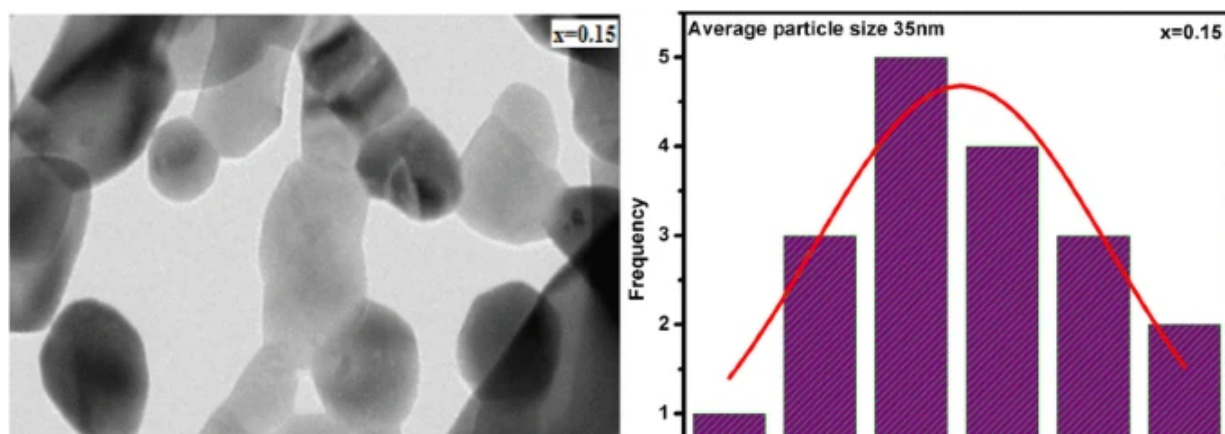
Fig. 5
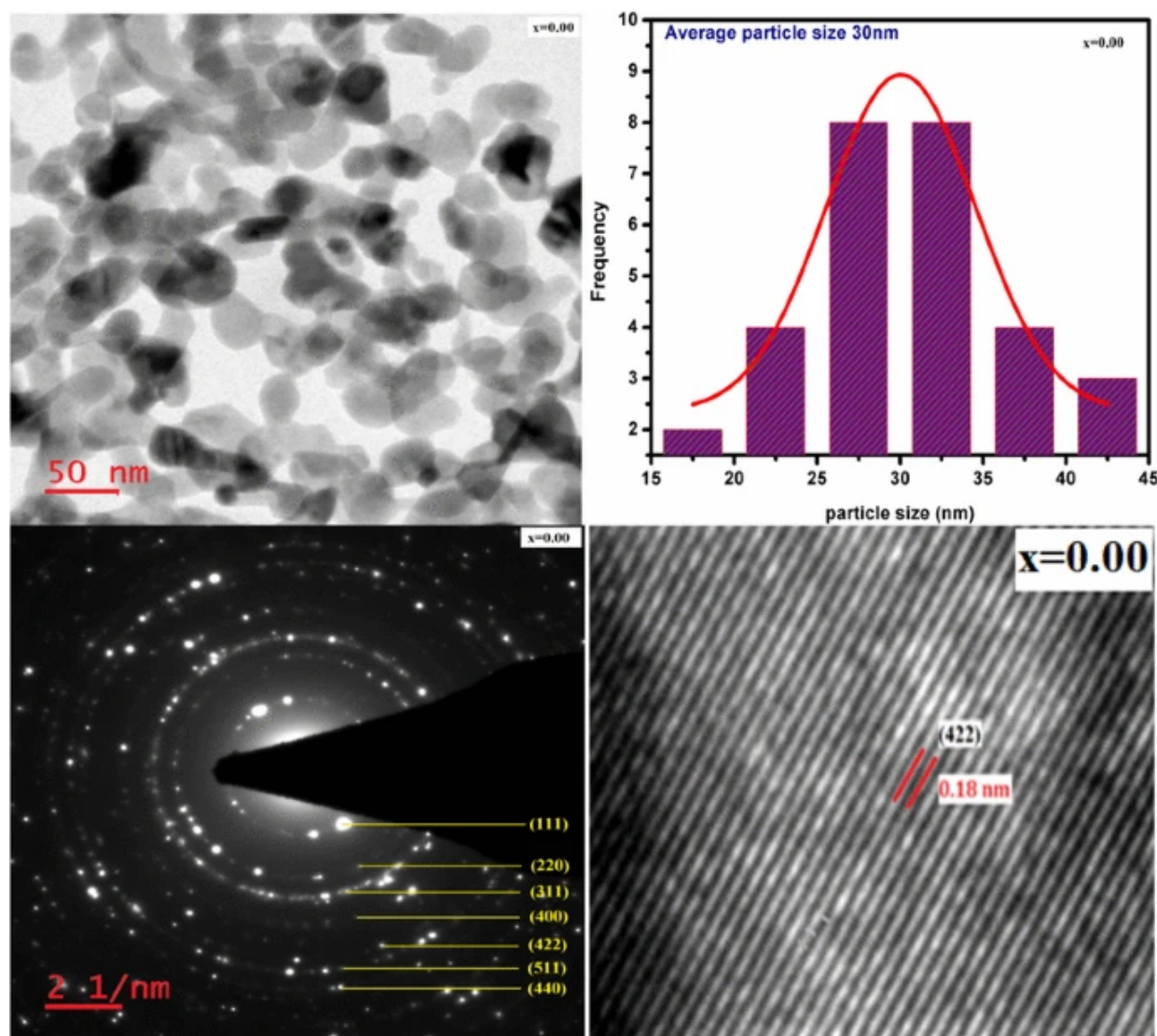
TEM images, histogram of particle size distribution, SAED pattern and HR–TEM for x = 0.00
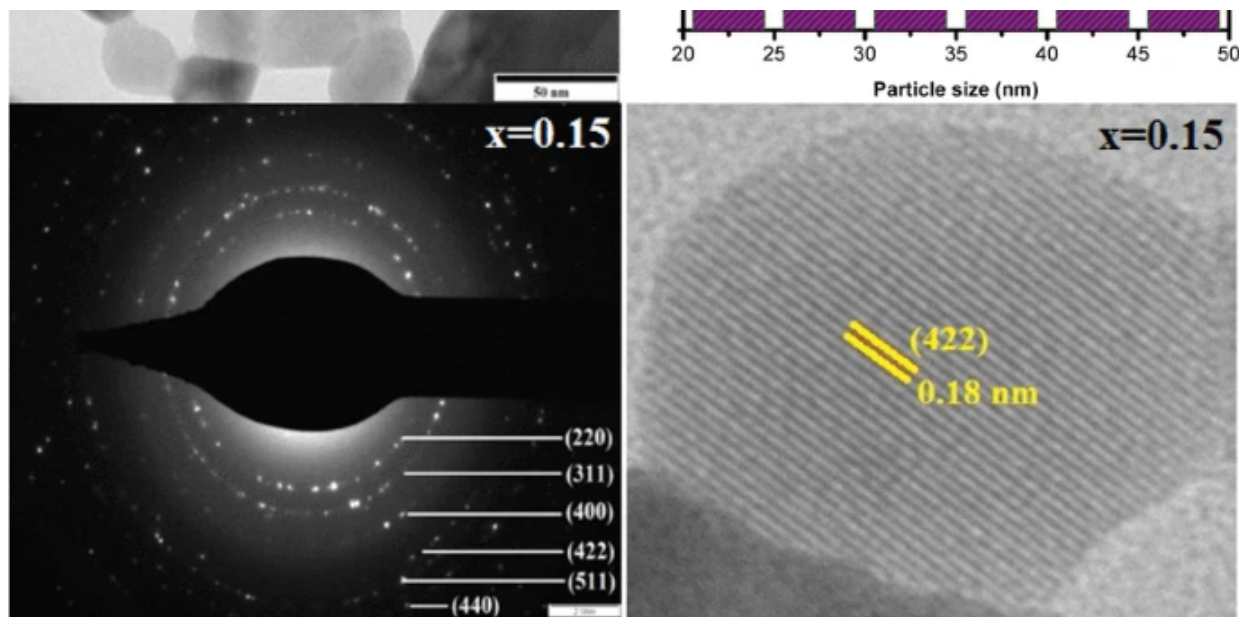
Fig. 6
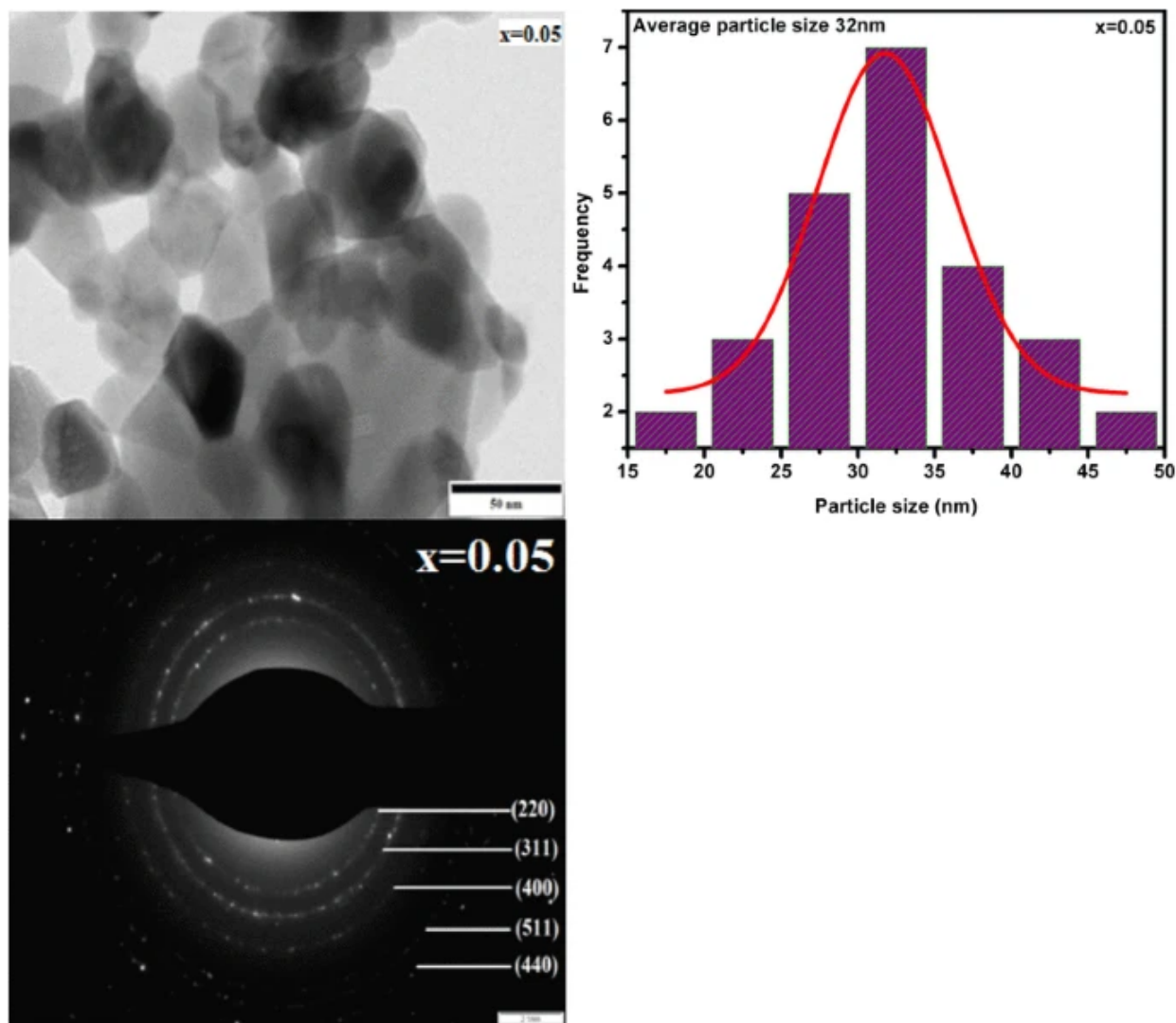
TEM images, histogram of particle size distribution, SAED pattern and HR–TEM for x = 0.05

Fig. 7

TEM images, histogram of particle size distribution, SAED pattern and HR-TEM for x = 0.15

4.4 Electrical studies

4.4.1 DC electrical resistivity

The DC electrical resistivity of $Ni_{0.70-x}Zn_{0.30}Fe_2O_4$ where x = 0.00, 0.05, 0.15 and 0.25 as a function of temperature was measured using two probe technique in the temperature range from room temperature to 850 k. The DC electrical resistivity is a vital property of ferrite, particularly for high-frequency applications wherein high resistivity is the pre-requisite. The resistivity of the spinel ferrites depends on porosity, grain size, density and sintering temperature.

The variation in room temperature resistivity as a function of copper content 'x' is plotted as shown in Fig. [8]. It is observed that as Cu^{2+} ions substitution increases room temperature DC resistivity also increases. The observed values of DC resistivity of parent sample (Ni–Zn ferrite) have nearly doubled upon the substitution of copper content from 0.0 to 0.25. This signifies that the nano ferrite with such high resistivity lead the low eddy current losses which are desirable for their applications in transformers, electromagnets, inductors and other electronic components. The observed behavior of resistivity of Ni–Zn ferrite with copper content 'x' can be explained on the basis of Verwey's hopping mechanism [33]. According to Verwey, in ferrites, the conduction occurs due to hopping of electrons between ions of the same element with different valence states (Fe^{3+} and Fe^{2+}) dispersed over crystallographically equivalent sub-lattices which results in space charge polarization. The hopping probability strongly influence by the concentration of Fe^{3+}/Fe^{2+} ion pairs at octahedral B-sites and activation energy. In parent sample $Ni_{0.70}Zn_{0.30}Fe_2O_4$, at octahedral B-site the concentration of $Fe^{3+}/$

Fe^{2+} is considered to be maximum. When Cu^{2+} is substituted, partial migration of Fe^{3+} ions from octahedral B-site will be took placed because of the occupancy preference of Cu^{2+} towards octahedral B-site. As a consequence, the number of Fe^{3+}/Fe^{2+} ions will be reduced by resulting a decrease in hopping of electrons thereby increasing resistivity. Another reason in resistivity enhancement can be increased activation energy (Table 2).

Fig. 8
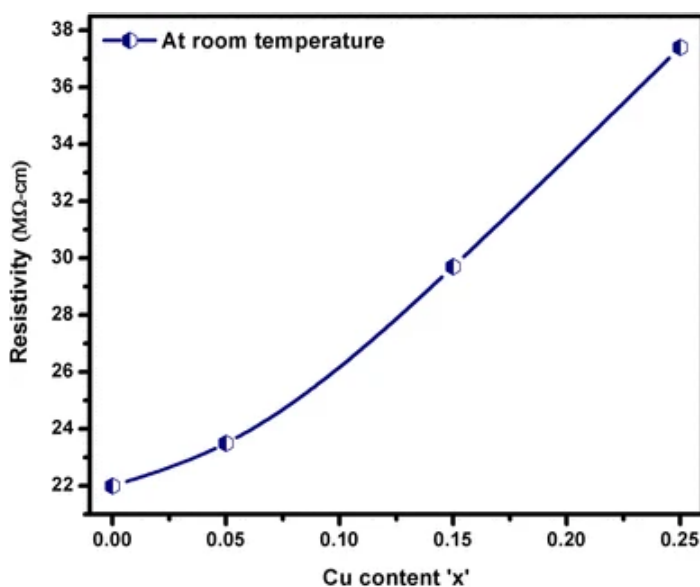
Variation of resistivity at room temperature with Cu concentration

Table 2 Activation energies in paramagnetic region (E_p), ferromagnetic region (E_f) and change in activation energy (ΔE), charge carrier concentration (n), and diffusion coefficient (D)

The plots of the log of resistivity (Ω cm) versus 1000/T (k^{-1}) called Arrhenius plot for all samples are shown in Fig. 9. It is observed from Arrhenius plots that the linear relation of DC resistivity has two distinct regions. Each region has its own conduction mechanism and different activation energy. The first region belongs to a ferrimagnetic phase which generally obeys the hopping mechanism and also called as the ordered region. The second region known as disordered region belongs to the paramagnetic phase. The change of magnetic order in ferrites from ferrimagnetic phase to paramagnetic phase is associated with the Curie point i.e. change in slope in DC electrical resistivity

plot has been reported by many researchers [34, 35]. Here, the Curie point was shifted to lower temperature upon substitution and increase in copper content 'x'. A similar behavior of Curie point was observed in divalent metal ion substituted spinel ferrite [36]. The value of Curie temperature for each sample is presented in Fig. 10. The decreasing behavior of Curie temperature can be explained on the basis of A–B exchange interaction due to the distribution of Fe^{3+} ions amongst available tetrahedral (A) and octahedral [B] sites. When copper substituted, according to site occupancy, Cu^{2+} might have entered to tetrahedral A-site, which displaces the Fe^{3+} ions from A-site to B-site. Thus, the weakening of A–B exchange interaction may occur which results in the increase of distance of moments between A and B sites. This is well supported by the increase of lattice parameter upon copper substitution. Hence, copper substitution has decreased the Curie temperature of NiCuZn nanocrystalline spinel ferrite.
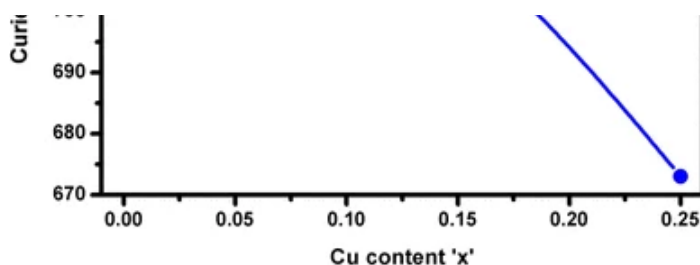
Fig. 9
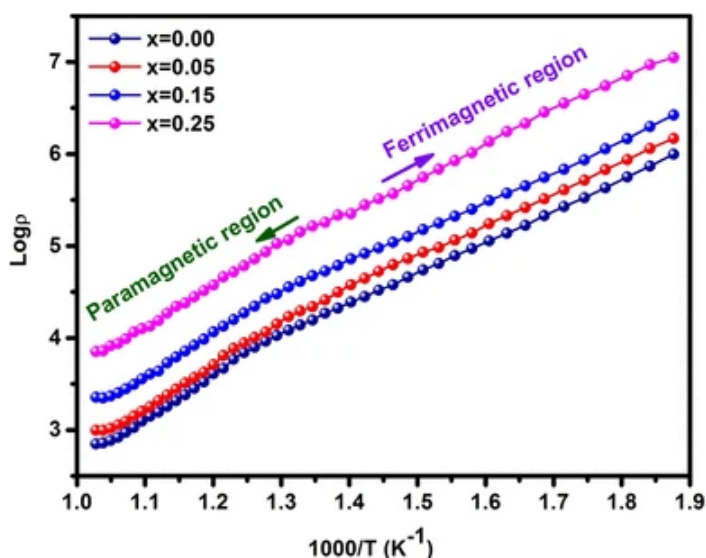
Arrhenuis plots as a function of temperature for $Ni_{0.70-x}Cu_xZn_{0.30}Fe_2O_4$ (x = 0.00, 0.05, 0.15 and 0.25)

Fig. 10
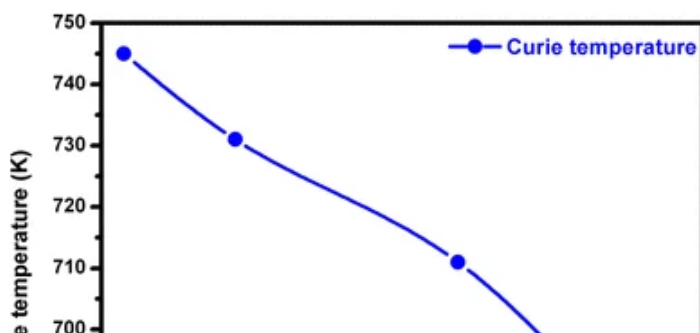
Compositional dependance of Curie temperature with copper content 'x'

The activation energy calculated using the standard relation [37] varies between 0.23 and 0.48 eV is tabulated in Table 2. The activation energy in both ferrimagnetic, as well as paramagnetic regions increases with copper substitution. Comparing both the activation energies it is evident that the activation energy of paramagnetic region is larger than that of the ferrimagnetic region. This indicates the influence of the change in the magnetic phase on the conduction in both regions. The activation energy is illustrated as a function of composition in Fig. 11. The behavior of activation energy can be explained in terms of jump length on octahedral site which was determined using XRD data. Activation energy and the hopping process may influence by jump length of the charge carriers at B-site. Figure 11 shows the increase in jump length with an increase in Cu contents. This causes an increase in activation energy required for jumping of charge carriers between sites.

Fig. 11
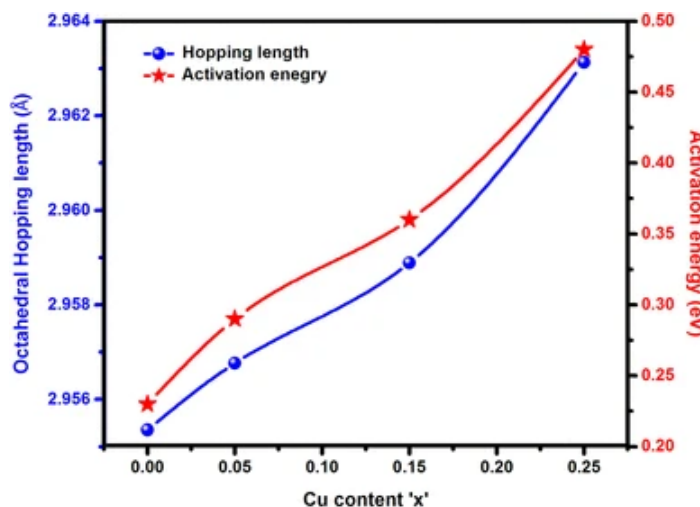
Variation of octahedral hopping length and activation energy as a function of copper content 'x'

The variation in resistivity at different temperatures with varying composition 'x' is presented in

Fig. [12]. It is evident from Fig. [12] that the DC electrical resistivity for x = 0.00, 0.05, 0.15 and 0.25 decreases as temperature increases suggesting the semiconducting behavior. Similar behavior of DC electrical resistivity as a function of temperature for nanocrystalline spinel ferrites has been reported [38], [39]. The decrease in DC electrical resistivity as a function of temperature can be attributed to the thermal mobility of charge carriers which increases as temperature increases. Thus, DC electrical resistivity decreases with increase in temperature.

Fig. 12
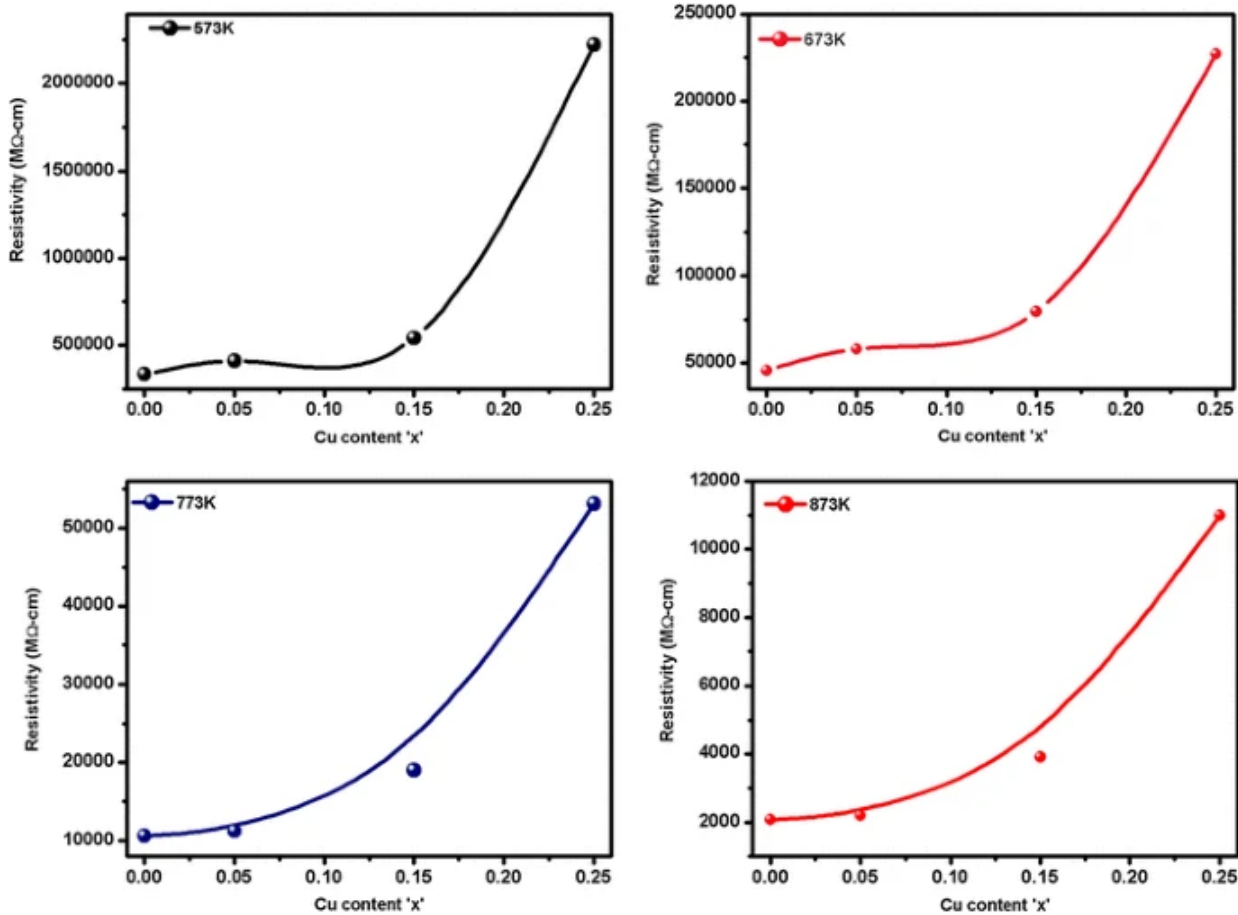
Variation of resistivity with Cu concentration at four different temperatures
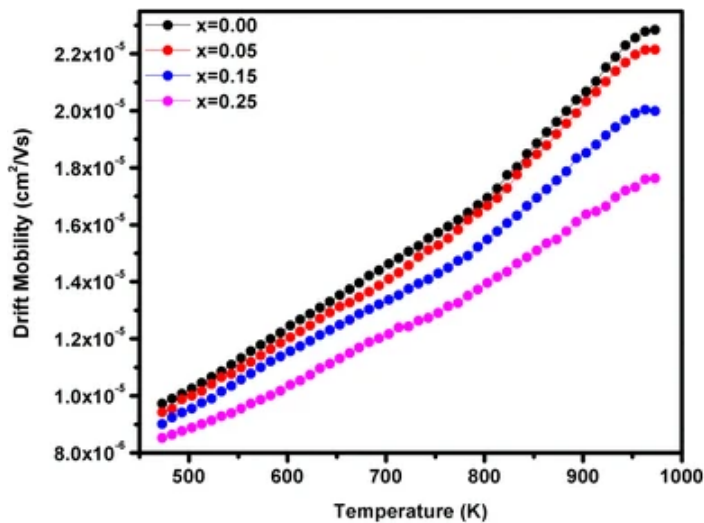
4.4.1.1 Drift mobility

The drift mobility of copper substituted Ni−Zn spinel ferrites was calculated using the following relation [40].

$${\mu _d}=\frac{1}{{ne\rho }}$$

(3)

where μ_d is the drift mobility, n is the charge carrier concentration, e is the charge on the electron and the ρ is the resistivity. The value of charge carrier concentration for each sample was obtained by a standard relation as given in [41] and presented in Table 2. The concentration of charge carriers with copper substitution was found to increase from 9.60×10^{22} to 9.98×10^{22} atoms/cm^3. The observed values of drift mobility for samples x = 0.00, 0.05, 0.15 and 0.25 are very small (2.28×10^{-5} to 8.52×10^{-6}). Such a small values of drift mobility for spinel ferrites are reported earlier by other researchers for various spinel ferrites [42, 43]. The plots of drift mobility (cm^2/Vs) versus temperature (K) are shown in Fig. 13. It is revealed from Fig. 13 that the charge carrier mobility increases as temperature increases. Moreover, Fig. 14 shows the variation in drift mobility with copper content 'x'. It is observed that the drift mobility as a function of copper content 'x' decreases which can be explained on the basis of increased charge carrier concentration.
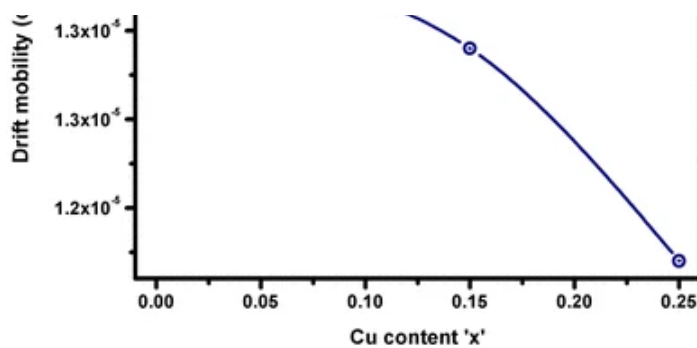
Fig. 13

Variation in drift mobility with temperature for Ni$_{0.70-x}$Cu$_x$Zn$_{0.30}$Fe$_2$O$_4$ (x = 0.00, 0.05, 0.15 and 0.25)

Fig. 14
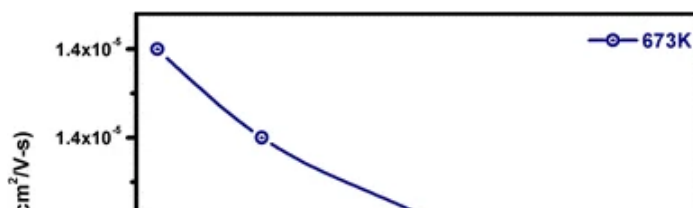
Compositional dependance of drift mobility with Cu at a specific temperature
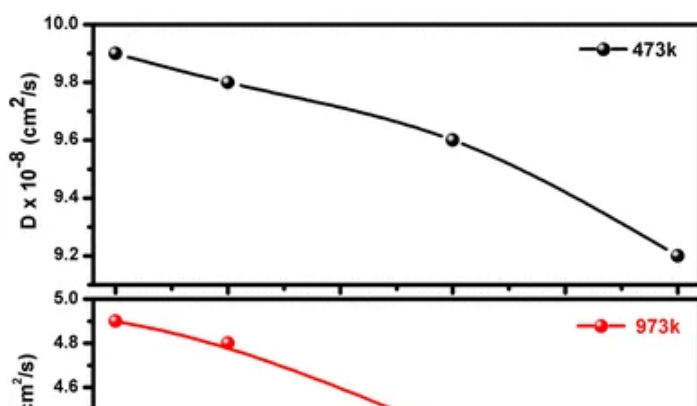
4.4.2 Diffusion coefficient

The diffusion coefficient as a function of temperature for each sample was evaluated by following relation [40]

$$D=\frac{{\sigma {k_B}T}}{{N{e^2}}}$$

(4)

where D is the diffusion coefficient, σ is the conductivity, k_B is the Boltzmann constant, T is the temperature, N is the number of atoms/cm^3 and e is the charge on the electron. The calculated values of diffusion coefficient for each sample at two different temperatures are summarized in Table 2. It is observed from Table 2 that the diffusion coefficient increases as temperature increases. Due to increase in conductivity with the temperature the diffusion coefficient increases. On the other hand, the diffusion coefficient decreases as presented in Fig. 15 for two different temperatures with copper content 'x'. This can be attributed to the creation of cation vacancy and reduction in oxygen vacancies upon copper substitution in the sub-lattice.

Fig. 15
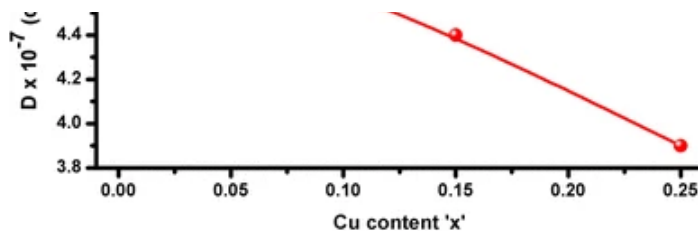
Variation of diffusion coeficient with Cu at two different temperatures

4.5 Dielectric properties

The dielectric response of Cu^{2+} substituted Ni−Zn spinel ferrite at room temperature with varying frequency was studied as dielectric constant and dielectric loss tangent.

4.6 Dielectric constant

The dielectric constant is of importance of high frequency devices. In ferrites, the dielectric constant is mainly contributed by electric, ionic, dipolar and interfacial polarizations. At low frequency around 1 kHz, dipolar and interfacial polarizations are principally important. The variation of dielectric constant over frequency range 50 Hz−1 MHz is depicted in Fig. 16.

Fig. 16
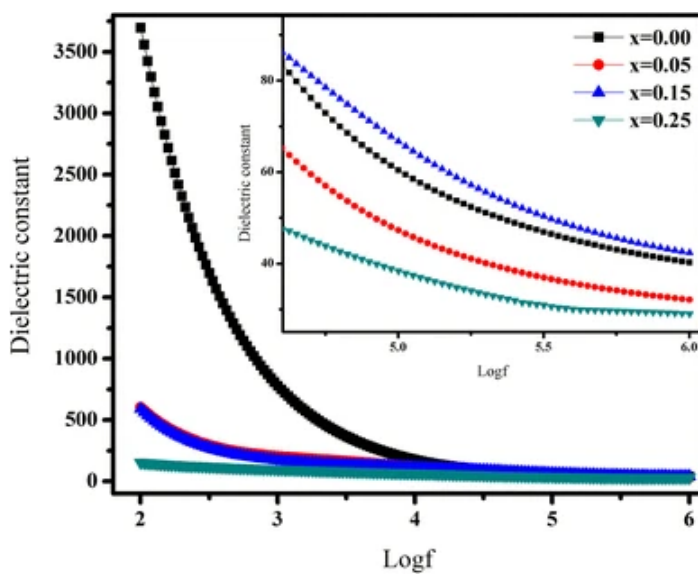
Variation of dielectric constant as a function of frequency

It reveals the large dispersion at low frequency which gradually changes in high frequency, indicates normal dielectric phenomenon. Similar behavior for other nanocrystalline spinel ferrites is reported [44]. It is noted that the dielectric constant decreases sharply at low frequency and getting slow down at high frequencies by attaining the almost constant value and become independent of frequency. The sharp decrease in response at low frequency is attributed to the polarization of cations. The high dielectric constant at low frequency can be explained on the basis of Maxwell−Wagner interfacial polarization model [45, 46] which depends on heterogeneous structure which consist grains with poor conductivity grain boundaries and is well consistent with Koops' theory [47]. It is a well-known fact that the grain boundaries with poor conductivity are highly active in low frequency and that of with good conductivity play a role in high frequency. This is the $\varepsilon_1 \approx \varepsilon_2$ reason the large dielectric constant observed at low frequency and low value of dielectric constant appear at high frequency. According to Koop's model, in polycrystalline ferrites the grains and grain boundaries are considered as one system. He had assumed

$$x = \frac{d_{2}}{d_{1}} \le 1,{\text{ }}\rho_{1} \le \rho_{2} \,{\text{and}}\,\varepsilon_{1} \approx \varepsilon_{2}$$

(5)

then, dielectric constant can be expressed as

$$\varepsilon^{\prime}=\frac{\varepsilon_1}{x} - \frac{\varepsilon_2}{x}$$

(6)

where x is the thickness of the grain boundary, ε_1 is a dielectric constant of grain and ε_2 is a dielectric constant of grain boundary, ρ_1 and ρ_2 are resistivity of grain and grain boundary respectively. Hence, the dielectric constant in low frequency is determined by grain boundary since the grain boundaries are more effective than the grains during electrical conduction. Thus, as thinner the boundary as, the larger the dielectric constant is. At higher frequency, the decrease in dielectric constant is attributed to the fact that the polarization decreases with increase in frequency. The polarization of the induced moments could not synchronize the frequency of externally applied electric field since the inhomogeneous dielectric structure requires a finite time for line up its axes in parallel to the applied external electric field. The electronic exchange between $Fe^{3+} \leftrightarrow Fe^{2+}$ lags behind the frequency of applied signal. Moreover, at higher frequencies, the dielectric constant is insensitive to heterogeneity. The observed low values of dielectric constant at high frequency (Fig. 16) are in close agreement with that of reported for spinel ferrites [48].

As shown in Fig. 17, dielectric constant decreases with copper substitution, exhibiting minimum with x = 0.25. The dielectric constant appeared in low frequency varied between 1138 and 152 for Cu^{2+} substituted samples and for Ni−Zn spinel ferrite sample it is (3696). This can be attributed to the substitution of copper ion in Ni−Zn spinel ferrite. Relatively low melting point of copper reduces the sintering temperature of Ni−Zn spinel ferrite, resulting, suppression of formation of Fe^{2+} as well as the polarization in ferrites. Thus, hopping of electrons between Fe^{2+} and Fe^{3+} decreases therefore, the dielectric constant decreases. However, the dielectric constant of composition x = 0.10 was found to increase slightly. It can be related to relatively low resistivity of that sample (Fig. 17). Moreover, Fig. 17 indicates that both DC resistivity at room temperature and dielectric constant at very low (50 Hz) frequency are complementary in nature. A large resistivity is corresponding to small dielectric constant while a small resistivity is corresponding to a large dielectric constant. This justifies the well-established fact that the dielectric behavior mainly governed by the conduction mechanism. The increased resistivity hinders the space charge carriers thereby impeding the space charge polarization. Thus, the dielectric constant decreases with increase in copper substitution.

Fig. 17
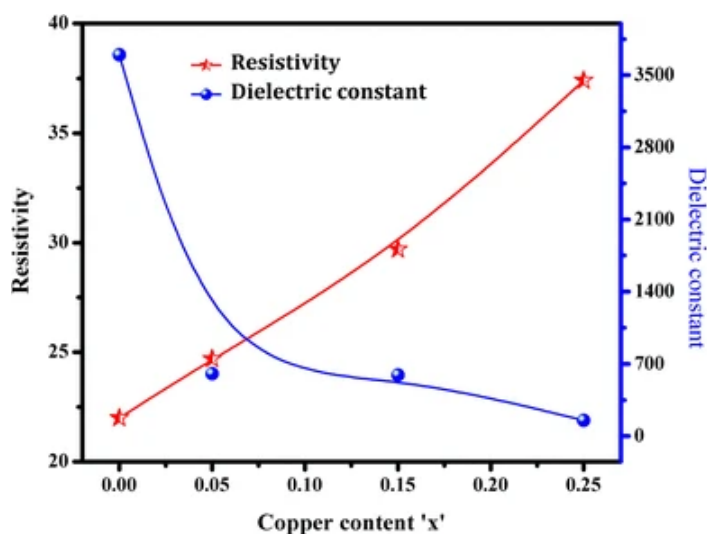
Compositional dependance of resistivity at room temperature and dielectric constant at 120 Hz
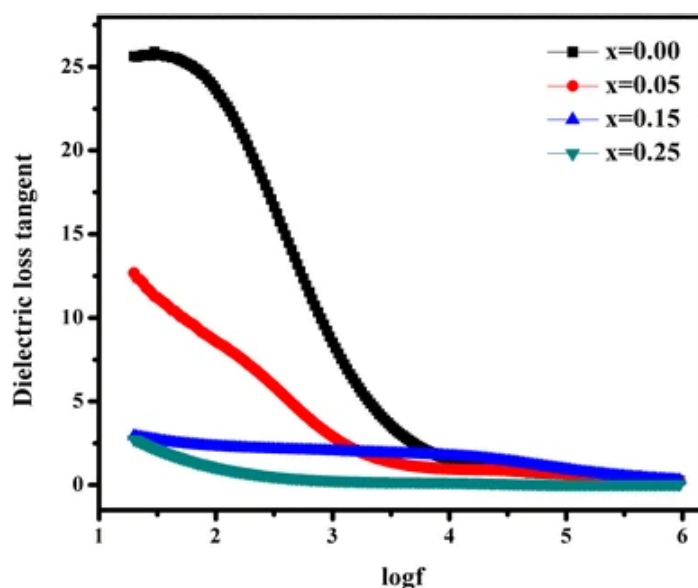
4.6.1 Dielectric loss tangent

The dielectric loss tangent represents the energy dissipation in the dielectric material which depends on various factors such as structural homogeneity, stoichiometry, and concentration of Fe^{2+} ions.

The variation on dielectric loss tangent with frequency is presented in Fig. 18. It is observed that the

dielectric loss tangent decreases exponentially with increase in frequency. It revealed the large dispersion at low frequency and decreases gradually at higher frequencies by attaining the almost constant values. It may be attributed to the conduction mechanism [49] in ferrites and the Maxwell–Wagner polarization model. If the frequency of applied signal is smaller than the hopping frequency of ions between $Fe^{3+} \leftrightarrow Fe^{2+}$ then the electrons follow the applied field hence the dielectric loss tangent at low frequency is maximum. Whereas at higher frequencies, minimum dielectric loss tangent is observed as the hopping frequency of ion exchange cannot follow the applied signal.

Fig. 18

Variation dielectric loss tangent as a function of frequency

Moreover, the dielectric loss tangent with copper concentration was found to decrease. The high frequency dependence of dielectric constant with copper substitution is shown in Fig. 18. It clearly shows that the dielectric loss of samples with increase in copper content at high frequency is much lower than that of in low frequency, suggesting the potential application of NiCuZn spinel ferrite in high frequency.

To summarize, high DC resistivity and low dielectric loss with potentially good magnetic behavior can make this material decidedly suitable for high frequency (few MHz) transformer cores, multilayer chip inductors, microwave devices etc.

5 Conclusions

Copper substituted Ni−Zn spinel ferrite was successfully prepared by nitrate-citrate route. The phase formation and purity checked by XRD patterns revealed the cubic spinel structure. Auxiliary confirmation of formation of ferrite skeleton was revealed by FTIR. The morphology investigated by SEM and TEM techniques suggested the porous foam-like, spherical nature with agglomerations. Arrhenius plots revealed the semiconducting nature of the studied samples. The activation energy and the DC electrical resistivity both enhanced with copper substitution. The dielectric constant and loss tangent both exponentially decayed with increase in frequency. Overall, copper substitution remarkably affects structural, electrical and dielectric properties of nanocrystalline Ni−Zn spinel ferrite.

References

1. N. Lee, T. Hyeon, Designed synthesis of uniformly sized iron oxide nanoparticles for efficient magnetic resonance imaging contrast agents. Chem. Soc. Rev. **41**, 2575−2589 (2012)

   Article **Google Scholar**

2. M. Mishra, A.P. Singh, B.P. Singh, V.N. Singh, S.K. Dhawan, Conducting ferrofluid: a high-performance microwave shielding material. J. Mater. Chem. A **2**, 13159−13168 (2014)

   Article **Google Scholar**

3. S. Mohapatra, S.R. Rout, S. Maiti, T.K. Maiti, A.B. Panda, Monodisperse mesoporous cobalt ferrite nanoparticles: synthesis and application in targeted delivery of antitumor drugs. J. Mater. Chem. **21**, 9185−9193 (2011)

   Article **Google Scholar**

4. A.R.O. Rodrigues, I.T. Gomes, B.G. Almeida, J.P. Araujo, E.M.S. Castanheira, P.J.G. Coutinho, Magnetic liposomes based on nickel ferrite nanoparticles for biomedical applications. Phys. Chem. Chem. Phys. **17**, 18011−18021 (2015)

   Article **Google Scholar**

5. Y. Yang, X. Liu, Y. Yang, W. Xiao, Z. Li, D. Xue et al., Synthesis of nonstoichiometric zinc ferrite nanoparticles with extraordinary room temperature magnetism and their diverse applications. J. Mater. Chem. C **1**, 2875–2885 (2013)

Article   **Google Scholar**

6. S.P. Dalawai, T.J. Shinde, A.B. Gadkari, P.N. Vasambekar, Ni–Zn ferrite thick film gas sensors. J. Mater. Sci.: Mater. Electron. **26**, 9016–9025 (2015)

Google Scholar

7. B.J. Rani, R. Mageswari, G. Ravi, V. Ganesh, R. Yuvakkumar, Physico-chemical properties of pure and zinc incorporated cobalt nickel mixed ferrite (ZnxCo0.005 − xNi0.005Fe2O4, where x = 0, 0.002, 0.004 M) nanoparticles. J. Mater. Sci.: Mater. Electron. (2017)

8. M. Hashim, S.E. Shirsath, S.S. Meena, M.L. Mane, S. Kumar, P. Bhatt et al., Manganese ferrite prepared using reverse micelle process: structural and magnetic properties characterization. J. Alloy. Compd. **642**, 70–77 (2015)

Article   **Google Scholar**

9. R. Kant Sharma, R. Ghose, Synthesis and characterization of nanocrystalline zinc ferrite spinel powders by homogeneous precipitation method. Ceram. Int. **41**, 14684–14691 (2015)

Article   **Google Scholar**

10. M. Liu, M. Lu, L. Wang, S. Xu, J. Zhao, H. Li, Mössbauer study on the magnetic properties and cation distribution of CoFe2O4 nanoparticles synthesized by hydrothermal method. J. Mater. Sci. **51**, 5487–5492 (2016)

Article   **Google Scholar**

11. K. Pemartin, C. Solans, J. Alvarez-Quintana, M. Sanchez-Dominguez, Synthesis of Mn–Zn ferrite nanoparticles by the oil-in-water microemulsion reaction method. Colloids Surf. A **451**, 161–171 (2014)

Article   **Google Scholar**

12. A.V. Raut, R.S. Barkule, D.R. Shengule, K.M. Jadhav, Synthesis, structural investigation and magnetic properties of Zn2 + substituted cobalt ferrite nanoparticles prepared by the sol−gel auto-combustion technique. J. Magn. Magn. Mater. **358−359**, 87−92 (2014)

Article   **Google Scholar**

13. J.S. Kounsalye, P.B. Kharat, M.V. Shisode, K. Jadhav, Influence of Ti4 + ion substitution on structural, electrical and dielectric properties of Li0. 5Fe2. 5O4 nanoparticles. J. Mater. Sci.: Mater. Electron. **2017**:1−8

14. C. Cao, A. Xia, S. Liu, L. Tong, Synthesis and magnetic properties of hydrothermal magnesium−zinc spinel ferrite powders. J. Mater. Sci.: Mater. Electron. **24**, 4901−4905 (2013)

Google Scholar

15. A. Najafi Birgani, M. Niyaifar, A. Hasanpour, Study of cation distribution of spinel zinc nano-ferrite by X-ray. J. Magn. Magn. Mater. **374**, 179−181 (2015)

Article   **Google Scholar**

16. M. Streckova, H. Hadraba, R. Bures, M. Faberova, P. Roupcova, I. Kubena et al., Chemical synthesis of nickel ferrite spinel designed as an insulating bilayer coating on ferromagnetic particles. Surf. Coat. Technol. **270**, 66−76 (2015)

Article   **Google Scholar**

17. Z.V. Mocanu, M. Airimioaei, C.E. Ciomaga, L. Curecheriu, F. Tudorache, S. Tascu et al., Investigation of the functional properties of Mg x Ni1−x Fe2O4 ceramics. J. Mater. Sci. **49**, 3276−3286 (2014)

Article   **Google Scholar**

18. M. Rahimi, P. Kameli, M. Ranjbar, H. Hajihashemi, H. Salamati, The effect of zinc doping on the

structural and magnetic properties of Ni1−x Zn x Fe2O4. J. Mater. Sci. **48**, 2969−2976 (2013)

Article   **Google Scholar**

19. V. Jeseentharani, L. Reginamary, B. Jeyaraj, A. Dayalan, K.S. Nagaraja, Nanocrystalline spinel Ni x Cu0.8−x Zn0.2Fe2O4: a novel material for humidity sensing. J. Mater. Sci. **47**, 3529−3534 (2012)

Article   **Google Scholar**

20. H. Su, H. Zhang, X. Tang, Y. Liu, Effects of nanocrystalline ferrite particles on densification and magnetic properties of the NiCuZn ferrites. J. Mater. Sci. **42**, 2849−2853 (2007)

Article   **Google Scholar**

21. V. Tsakaloudi, D. Sakellari, V. Zaspalis, E.K. Polychroniadis, Stress relaxation phenomena in NiCuZn ferrites induced by annealing. J. Mater. Sci. **48**, 3692−3699 (2013)

Article   **Google Scholar**

22. G. Sathishkumar, C. Venkataraju, K. Sivakumar, Effect of nickel on the structural and magnetic properties of nano structured CoZnFe2O4. J. Mater. Sci.: Mater. Electron. **22**, 1715 (2011)

Google Scholar

23. R. Maleque, M.D. Rahaman, A.K.M. Akther Hossain, Influence of Ca2+ ions substitution on structural, microstructural, electrical and magnetic properties of Mg0.2−xCaxMn0.5Zn0.3Fe2O4 ferrites. J. Mater. Sci.: Mater. Electron. **28**, 13185−13200 (2017)

Google Scholar

24. K. Modi, Elastic moduli determination through IR spectroscopy for zinc substituted copper ferri chromates. J. Mater. Sci. **39**, 2887−2890 (2004)

Article   **Google Scholar**

25. A. Sutka, G. Mezinskis, Sol-gel auto-combustion synthesis of spinel-type ferrite nanomaterials.

Front. Mater. Sci. **6**, 128−141 (2012)

Article **Google Scholar**

26. I.P. Muthuselvam, R.N. Bhowmik, Mechanical alloyed Ho3+ doping in CoFe2O4 spinel ferrite and understanding of magnetic nanodomains. J. Magn. Magn. Mater. **322**, 767−776 (2010)

Article **Google Scholar**

27. G. Luo, W. Zhou, J. Li, G. Jiang, S. Tang, Y-w. Du, Effect of Cu ion substitution on structural and dielectric properties of Ni−Zn ferrites. Trans. Nonferrous Metals Soc. China **25**, 3678−3684 (2015)

Article **Google Scholar**

28. L. Khanna, N.K. Verma, PEG/CaFe2O4 nanocomposite: structural, morphological, magnetic and thermal analyses. Phys. B **427**, 68−75 (2013)

Article **Google Scholar**

29. G.H. Kale, A.V. Humbe, S.D. Birajdar, A.B. Shinde, K.M. Jadhav, l-Ascorbic acid assisted synthesis and characterization of CoFe2O4 nanoparticles at different annealing temperatures. J. Mater. Sci.: Mater. Electron. **27**, 2151−2158 (2016)

Google Scholar

30. K.B. Modi, S.J. Shah, N.B. Pujara, T.K. Pathak, N.H. Vasoya, I.G. Jhala, Infrared spectral evolution, elastic, optical and thermodynamic properties study on mechanically milled Ni0.5Zn0.5Fe2O4 spinel ferrite. J. Mol. Struct. **1049**, 250−262 (2013)

Article **Google Scholar**

31. G. Padmapriya, A. Manikandan, V. Krishnasamy, S.K. Jaganathan, S.A. Antony, Spinel NixZn1−xFe2O4 (0.0 ≤ x ≤ 1.0) nano-photocatalysts: synthesis, characterization and photocatalytic degradation of methylene blue dye. J. Mol. Struct. **1119**, 39−47 (2016)

Article **Google Scholar**

32. S.E. Shirsath, M.L. Mane, Y. Yasukawa, X. Liu, A. Morisako, Self-ignited high temperature synthesis and enhanced super-exchange interactions of Ho3+−Mn2+−Fe3+−O2− ferromagnetic nanoparticles. Phys. Chem. Chem. Phys. **16**, 2347−2357 (2014)

Article **Google Scholar**

33. M. Raghasudha, D. Ravinder, P. Veerasomaiah, Electrical resistivity studies of Cr doped Mg nano-ferrites. Mater. Discov. **2**, 50−54 (2015)

Article **Google Scholar**

34. S.R. Nimbore, D.R. Shengule, S.J. Shukla, G.K. Bichile, K.M. Jadhav, Magnetic and electrical properties of lanthanum substituted yttrium iron garnets. J. Mater. Sci. **41**, 6460−6464 (2006)

Article **Google Scholar**

35. V.S. Sawant, A.A. Bagade, K.Y. Rajpure, Studies on structural and electrical properties of Li0.5 − 0.5xCoxFe2.5−0.5xO4 (0 ≤ x ≤ 0.6) spinel ferrite. Phys. B **474**, 47−52 (2015)

Article **Google Scholar**

36. V. Vinayak, P.P. Khirade, S.D. Birajdar, R.C. Alange, K.M. Jadhav, Electrical and dielectrical Properties of low-temperature-synthesized nanocrystalline Mg2+−substituted cobalt spinel ferrite. J. Supercond. Novel Magn. **28**, 3351−3356 (2015)

Article **Google Scholar**

37. A.M. Abdeen, O.M. Hemeda, E.E. Assem, M.M. El-Sehly, Structural, electrical and transport phenomena of Co ferrite substituted by Cd. J. Magn. Magn. Mater. **238** 75−83 (2002)

Article   **Google Scholar**

38. W. Bayoumi, Structural and electrical properties of zinc-substituted cobalt ferrite. J. Mater. Sci. **42**, 8254−8261 (2007)

Article   **Google Scholar**

39. A.D. Sheikh, V.L. Mathe, Anomalous electrical properties of nanocrystalline Ni−Zn ferrite. J. Mater. Sci. **43**, 2018−2025 (2008)

Article   **Google Scholar**

40. D.R.K.B. Ravinder, Electrical conductivity of cerium substituted Mn−Zn ferrites. Mater. Lett. **57**, 1738−1742 (2003)

Article   **Google Scholar**

41. A.V. Humbe, A.C. Nawle, A.B. Shinde, K.M. Jadhav, Impact of Jahn Teller ion on magnetic and semiconducting behaviour of Ni−Zn spinel ferrite synthesized by nitrate-citrate route. J. Alloy. Compd. **691**, 343−354 (2017)

Article   **Google Scholar**

42. D. Bahadur, O.M. Parkash, D. Kumar, Bull. Mater. Sci. **3**, 325−331 (1981)

Article   **Google Scholar**

43. O.M. Hameda, J. Magn. Magn. Mater. **256**, 63−68 (2003)

Article   **Google Scholar**

44. E. Ranjith Kumar, P. Siva Prasada Reddy, G. Sarala Devi, S. Sathiyaraj, Structural, dielectric and gas sensing behavior of Mn substituted spinel MFe2O4 (M = Zn, Cu, Ni, and Co) ferrite nanoparticles. J. Magn. Magn. Mater. **398**, 281−288 (2016)

Article   **Google Scholar**

45. B.P. Rao, K.H. Rao, Effect of sintering conditions on resistivity and dielectric properties of Ni−Zn ferrites. J. Mater. Sci. **32**, 6049−6054 (1997)

Article   **Google Scholar**

46. J.C. Maxwell, *A Treatise on Electricity and Magnetism*. Clarendon Press 1873

47. C.G. Koops, On the dispersion of resistivity and dielectric constant of some semiconductors at audiofrequencies. Phys. Rev. **83**, 121−124 (1951)

Article   **Google Scholar**

48. K. Iwauchi, Dielectric properties of fine particles of Fe3O4 and some ferrites. Jpn. J. Appl. Phys. **10**, 1520−1528 (1971)

Article   **Google Scholar**

49. E.J. Verwey, P.W. Haayman, F.C. Romeijn, Physical properties and cation arrangement of oxides with spinel structures II. Electronic conductivity. J. Chem. Phys. **15**, 181−187 (1947)

Article   **Google Scholar**

Acknowledgements

Author information

Authors and Affiliations

Department of Physics, Dr. Babasaheb Ambedkar Marathwada University, Aurangabad, Maharashtra, 431004, India

Ashok V. Humbe, Prashant B. Kharat & K. M. Jadhav

Department of Physics, Vivekanand Arts, Sardar Dalipsingh Commerce and Science College, Aurangabad, Maharashtra, 431004, India

Anant C. Nawle

Corresponding author

Correspondence to Ashok V. Humbe.

Rights and permissions

Reprints and permissions

About this article

Cite this article

Share this article

Anyone you share the following link with will be able to read this content:

Get shareable link

Provided by the Springer Nature SharedIt content–sharing initiative